

Optimized detection modality for double resonance alignment based optical magnetometer

A. Akbar^{1,*}, M. Koźbial², L. Elson¹, A. Meraki¹, J. Kołodyński² and K. Jensen^{1,†}

¹*School of Physics and Astronomy, University of Nottingham,
University Park, Nottingham, NG7 2RD, UK*

²*Centre for Quantum Optical Technologies, Centre of New Technologies,
University of Warsaw, Banacha 2c, 02-097 Warszawa, Poland*

In this work, we present a comprehensive and comparative analysis of two detection modalities, i.e., polarization rotation and absorption measurement of light, for a double resonance alignment based optical magnetometer (DRAM). We derive algebraic expressions for magnetometry signals based on multipole moments description. Experiments are carried out using a room-temperature paraffin-coated Caesium vapour cell and measuring either the polarization rotation or absorption of the transmitted laser light. A detailed experimental analysis of the resonance spectra is performed to validate the theoretical findings for various input parameters. The results signify the use of a single isotropic relaxation rate thus simplifying the data analysis for optimization of the DRAM. The sensitivity measurements are performed and reveal that the polarization rotation detection mode yields larger signals and better sensitivity than absorption measurement of light.

I. INTRODUCTION

Optically pumped magnetometers (OPMs) [1–3] based on alkali atom vapours have been instrumental in the advancement of diverse fields including magnetoencephalography (MEG) [4–8], biomagnetism [9–12], paleomagnetism [13], remote object detection [14, 15] and dark matter research [16, 17]. The recent increase in the scope of OPMs can be attributed to their non-destructive, remote sensing capabilities to measure weak magnetic fields in the range of $\text{fT}/\sqrt{\text{Hz}}$ [18] which were possible earlier only with superconducting quantum interference device (SQUID) magnetometers operating at cryogenic temperatures [19]. The technological advancement in the field of optical magnetometry has led to the enhanced sensitivity ($\text{sub-fT}/\sqrt{\text{Hz}}$), miniaturization, robust wearable capabilities of the OPMs and has potentially opened up new avenues in medical science to be explored [20–23].

OPMs have been investigated as a double resonance optical magnetometer [24] which can be used as a scalar magnetometer for e.g. measuring the Earth’s magnetic field amplitude, or for detecting oscillating/radio-frequency (RF) magnetic fields [25, 26]. In a double resonance optical magnetometer, light is used for polarizing the atomic spins using the process of optical pumping. The spins are then driven by a RF-field $\mathbf{B}_{\text{rf}}(t)$ creating precession of the spin-polarization around a static magnetic field \mathbf{B}_0 . In a double resonance orientation magnetometer (DROM), circular polarized light is used to orient the atomic spins in a certain direction. On

the other hand, in a double resonance alignment magnetometer (DRAM), linear polarized light is used to align the atomic spins along a certain axis [27]. In both cases, the spin-precession will induce periodic modulations in the measured observables, i.e., the absorption or polarization rotation of the transmitted light. These modulations will in turn generate signals at first and/or second harmonic of the applied RF frequency. The alignment based magnetometer has been utilized previously for detection of RF fields [28, 29], for zero-field magnetometry [30], vector magnetometry [31] and also for spin noise spectroscopy [32].

The theoretical description of DROM and DRAM for the evolution of spin polarized system is based on a three step model: pump, evolve and probe. The model is valid for arbitrary RF intensities at low light power, i.e., optical pumping rate is smaller than the relaxation rate such that the system reaches a steady state. Previous works has mainly considered probing of a DRAM through absorption measurement of the transmitted light [27].

In this work, we extend the theoretical approach for DRAM to another detection modality, i.e., the measurement of the polarization rotation of the transmitted light. We derive the algebraic expressions characterizing the in-phase and quadrature lineshapes where magnetic resonance spectra is observed through rotation of the linear polarization of light (Sec. II A). Consequently, we performed detailed experimental investigations to explore the dependence of magnetic resonance signal on various parameters to validate the theoretical findings. The detailed analysis for RF intensity, light power and angular dependence of resonance spectra is presented in Section IV. Furthermore, magnetic field sensitiv-

* ali.akbar@nottingham.ac.uk

† kasjensendk@gmail.com

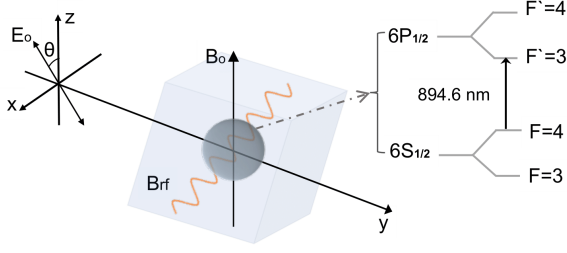


Figure 1: (a) Illustration of the DRAM geometry where linearly polarized light interacts with Caesium (Cs) atomic vapours in the presence of a static and oscillating magnetic field. (b) Caesium level scheme. The laser light is tuned to the D1 = 894.6 nm transition.

ity measurements are performed and results are presented in Section IV D. We also present the results for absorption measurements in parallel to draw a comprehensive comparison between the two detection techniques. This work highlights the advantage of utilizing the polarization based detection mode. The results demonstrate that the polarization rotation-based detection outperforms the conventional absorption measurements in terms of magnetic field sensitivity within the DRAM geometry.

II. THEORETICAL DESCRIPTION OF DRAM GEOMETRY

A. DRAM geometry

Fig. 1 illustrates the DRAM geometry. Laser light propagating in the $\mathbf{k}||\hat{y}$ direction and linearly polarized in the $\hat{\mathbf{e}} = \cos(\theta)\hat{\mathbf{z}} + \sin(\theta)\hat{\mathbf{x}}$ direction at an angle θ in the zx -plane is incident on an atomic vapour cell. The linearly polarized light creates a spin-alignment of atomic vapour which evolves in the combined presence of a static \mathbf{B}_0 and an oscillating weak magnetic field $\mathbf{B}_{\text{rf}}(t)$ such that the spin-aligned media will precess around the static magnetic field. The atomic state can be detected by measuring the absorption or the change in polarization of the transmitted light. The signal will oscillate at frequencies at the first and second harmonics of the RF field.

B. Description of the atomic state

Our experiments are carried out using room-temperature Caesium (Cs) atomic vapour contained in a 5 mm cubic paraffin-coated glass cell. Caesium has two ground states with hyperfine quantum numbers $F = 3$ and $F = 4$ and first excited states with $F' = 3$ and $F' = 4$ as shown in

Fig. 1. The laser light has wavelength 894.6 nm and is resonant with the $F = 4 \rightarrow F' = 3$ D1 transition. We consider atoms in the $F = 4$ ground state which has $2F + 1$ magnetic sub-levels $|F, M\rangle$ (using the z -axis as quantization direction) as only those atoms are probed by the light. A single atom with the hyperfine quantum number F can be described by the density matrix with eigenbasis \hat{F}^2, \hat{F}_z and can be written as

$$\rho = \sum_{M, M'=-F}^F \rho_{MM'}^{(F)} |F, M\rangle \langle F, M'|. \quad (1)$$

It is instructive to write the density matrix in the basis of spherical tensor operators

$$\rho = \sum_{\kappa=0}^{2F} \sum_{q=-\kappa}^{\kappa} m_{\kappa,q} \tau_q^{(\kappa)}, \quad (2)$$

where $m_{\kappa,q}$ are multipole components with rank $\kappa = 0, 1, \dots, 2F$ and $q = -\kappa, \dots, \kappa$ and $\tau_q^{(\kappa)}$ are irreducible spherical tensor operators [27, 33]. For $\kappa = 1$, multipoles describe the orientation of the spin whereas $\kappa = 2$ describes how the spins are aligned along some axis. We can organize the rank 2 alignment multipoles in a column vector

$$\mathbf{m}_2 = (m_{2,-2}, m_{2,-1}, m_{2,0}, m_{2,1}, m_{2,2})^T, \quad (3)$$

where T denotes the transpose of matrix.

Optical pumping with light polarized along the z -direction will create the alignment

$$\mathbf{m}_2^{\text{eq}} = (0, 0, m_{2,0}^{\text{ini}}, 0, 0)^T. \quad (4)$$

If the light is instead polarized at an angle θ in the zx -plane, as illustrated in Fig. 1, we have

$$\mathbf{m}_2^{\text{eq}}(\theta) = (0, 0, m_{2,0}^{\text{ini}} [1 + 3 \cos(2\theta)] / 4, 0, 0)^T, \quad (5)$$

which can be calculated by rotating the multipole given in Eq. 4 by an angle $-\theta$ around the y -axis and assuming that multipoles with $q \neq 0$ average to zero as we do not consider the pulsed optical pumping.

C. Evolution of the atomic state

We now calculate the evolution of the alignment multipoles in the presence of the magnetic field $B_0 \hat{\mathbf{z}} + B_{\text{rf}} \cos(\omega_{\text{rf}} t) \hat{\mathbf{x}}$. The unitary evolution is governed by the equation

$$\dot{\mathbf{m}}_2 = \left(-i\omega_L J_z^{(2)} - i\Omega_{\text{rf}} \cos(\omega_{\text{rf}} t) J_x^{(2)} \right) \mathbf{m}_2, \quad (6)$$

where $\omega_L = \gamma_F B_0 / \hbar$ is the Larmor frequency, $\Omega_{\text{rf}} = \gamma_F B_{\text{rf}} / \hbar$ is the Rabi frequency of the RF

field, and γ_F is the gyromagnetic ratio. The matrices $J_x^{(2)}$ and $J_z^{(2)}$ are the relevant representation of the angular momentum operators, which are written out in matrix form in Appendix A.

We now define variables in the rotating frame with frequency ω_{rf}

$$\tilde{m}_{\kappa,q} = e^{iq\omega_{\text{rf}}t} m_{\kappa,q}, \quad (7)$$

or equivalently written using vector notation

$$\tilde{\mathbf{m}}_2 = \mathbf{R}_z^{(2)}(-\omega_{\text{rf}}t) \mathbf{m}_2, \quad (8)$$

where

$$\mathbf{R}_z^{(2)}(-\omega_{\text{rf}}t) = \exp\left(i\omega_{\text{rf}}t J_z^{(2)}/\hbar\right) \quad (9)$$

is the rotation matrix around the z axis generated by the relevant angular momentum representation. Assuming the rotating wave approximation, the rotating frame multipoles will evolve according to

$$\dot{\tilde{\mathbf{m}}}_2 = \left(i\delta J_z^{(2)} - i\frac{\Omega_{\text{rf}}}{2} J_x^{(2)}\right) \tilde{\mathbf{m}}_2 - \Gamma \tilde{\mathbf{m}}_2 + \Gamma \tilde{\mathbf{m}}_2^{\text{eq}}, \quad (10)$$

where $\delta = \omega_{\text{rf}} - \omega_L$ is the detuning of the RF field from the Larmor frequency. We have furthermore included terms describing optical pumping and ground state relaxation in the equation, and for simplicity assumed relaxation can be described by a single rate Γ . Equation 10 can be solved in the steady state where $\dot{\tilde{\mathbf{m}}}_2 = 0$ yielding the solution $\tilde{\mathbf{m}}_2^{\text{ss}}$ which is explicitly written out in Appendix B.

D. Polarization rotation signal

The observable signals depend on the multipoles \mathbf{m}'_2 that are defined with quantization axis in the light-polarization $\hat{\mathbf{e}}$ direction. They are related to the lab frame multipoles \mathbf{m}_2 and one can calculate the other by applying a rotation with the angle θ , i.e.

$$\mathbf{m}'_2 = \mathbf{R}_y^{(2)}(\theta) \mathbf{m}_2, \quad (11)$$

where the rotation matrix around the y -axis with the angle θ is

$$\mathbf{R}_y^{(2)}(\theta) = \exp\left(-i\theta J_y^{(2)}/\hbar\right). \quad (12)$$

Using the definition of the rotating frame, we furthermore have

$$\mathbf{m}'_2 = \mathbf{R}_y^{(2)}(\theta) \mathbf{R}_z^{(2)}(+\omega_{\text{rf}}t) \tilde{\mathbf{m}}_2. \quad (13)$$

We first consider the light polarization rotation signal which for light propagating in the y -direction can be calculated using the methods of [30] as

$$S^{\text{PR}}(t) \propto [m'_{2,-1}(t) - m'_{2,1}(t)]. \quad (14)$$

Inserting the rotating frame steady state solutions given in App. B into Eq. 13, and calculating the polarization rotation signal given by Eq. 14, we find that the signal has three contributions

$$S^{\text{PR}}(t) \propto S_0^{\text{PR}}(t) + S_1^{\text{PR}}(t) + S_2^{\text{PR}}(t), \quad (15)$$

which are oscillating at frequencies 0, ω_{rf} and $2\omega_{\text{rf}}$, respectively. We can compactly write the signal as

$$S_0^{\text{PR}}(t) \propto h_0(\theta) A_0, \quad (16)$$

$$S_1^{\text{PR}}(t) \propto h_1(\theta) [D_1 \cos(\omega_{\text{rf}}t) + A_1 \sin(\omega_{\text{rf}}t)], \quad (17)$$

$$S_2^{\text{PR}}(t) \propto h_2(\theta) [A_2 \cos(2\omega_{\text{rf}}t) + D_2 \sin(2\omega_{\text{rf}}t)], \quad (18)$$

where the angular dependence takes the form

$$h_0(\theta) = \sin(2\theta)[1 + 3\cos(2\theta)], \quad (19a)$$

$$h_1(\theta) = \cos(2\theta)[1 + 3\cos(2\theta)], \quad (19b)$$

$$h_2(\theta) = \sin(2\theta)[1 + 3\cos(2\theta)]. \quad (19c)$$

The in-phase and quadrature line shapes for the first harmonic signal take the form

$$A_1(\delta, \Omega_{\text{rf}}) = \frac{\sqrt{\frac{3}{2}} m_{2,0}^{\text{ini}} \Gamma \Omega_{\text{rf}} [4(\Gamma^2 + 4\delta^2) + \Omega_{\text{rf}}^2]}{4(\Gamma^2 + 4\delta^2 + \Omega_{\text{rf}}^2) [4(\Gamma^2 + \delta^2) + \Omega_{\text{rf}}^2]}, \quad (20)$$

$$D_1(\delta, \Omega_{\text{rf}}) = -\frac{\sqrt{\frac{3}{2}} m_{2,0}^{\text{ini}} \delta \Omega_{\text{rf}} [2(\Gamma^2 + 4\delta^2) - \Omega_{\text{rf}}^2]}{2(\Gamma^2 + 4\delta^2 + \Omega_{\text{rf}}^2) [4(\Gamma^2 + \delta^2) + \Omega_{\text{rf}}^2]}. \quad (21)$$

On resonance, the amplitude of the first harmonic signal $R_1 = \sqrt{A_1^2 + D_1^2}$ will be

$$R_1(\delta = 0, \Omega_{\text{rf}}) = \frac{\sqrt{\frac{3}{2}} m_{2,0}^{\text{ini}} \Gamma \Omega_{\text{rf}}}{4(\Gamma^2 + \Omega_{\text{rf}}^2)}. \quad (22)$$

We see that the first harmonic signal is proportional to the RF intensity Ω_{rf} for small amplitude of Ω_{rf} . In the limit of low RF intensities, Eq. (20) and Eq. (21) reduce to

$$A_1(\delta, \Omega_{\text{rf}} \approx 0) = \frac{1}{4} \sqrt{\frac{3}{2}} m_{2,0}^{\text{ini}} \frac{\Gamma \Omega_{\text{rf}}}{\Gamma^2 + \delta^2}, \quad (23)$$

$$D_1(\delta, \Omega_{\text{rf}} \approx 0) = -\frac{1}{4} \sqrt{\frac{3}{2}} m_{2,0}^{\text{ini}} \frac{\delta \Omega_{\text{rf}}}{\Gamma^2 + \delta^2}, \quad (24)$$

$$R_1(\delta, \Omega_{\text{rf}} \approx 0) = \frac{1}{4} \sqrt{\frac{3}{2}} m_{2,0}^{\text{ini}} \frac{\Omega_{\text{rf}}}{\sqrt{\Gamma^2 + \delta^2}}. \quad (25)$$

We also calculate the signal at the second har-

monic

$$A_2(\delta, \Omega_{\text{rf}}) = \frac{\sqrt{\frac{3}{2}} m_{2,0}^{\text{ini}} \Omega_{\text{rf}}^2 [4(\Gamma^2 - 2\delta^2) + \Omega_{\text{rf}}^2]}{16(\Gamma^2 + 4\delta^2 + \Omega_{\text{rf}}^2) [4(\Gamma^2 + \delta^2) + \Omega_{\text{rf}}^2]}, \quad (26)$$

$$D_2(\delta, \Omega_{\text{rf}}) = \frac{3\sqrt{\frac{3}{2}} m_{2,0}^{\text{ini}} \Omega_{\text{rf}}^2 \Gamma \delta}{4(\Gamma^2 + 4\delta^2 + \Omega_{\text{rf}}^2) [4(\Gamma^2 + \delta^2) + \Omega_{\text{rf}}^2]}. \quad (27)$$

On resonance, the second harmonic signal is

$$R_2(\delta = 0, \Omega_{\text{rf}}) = \frac{\sqrt{\frac{3}{2}} m_{2,0}^{\text{ini}} \Omega_{\text{rf}}^2}{16(\Gamma^2 + \Omega_{\text{rf}}^2)}. \quad (28)$$

For $\Omega_{\text{rf}} \ll \Gamma$, the signal at the second harmonic is proportional to the square of the RF intensity Ω_{rf}^2 . In the limit of low RF intensities Eqs. (26) and (27) simplify to

$$A_2(\delta, \Omega_{\text{rf}} \approx 0) = \frac{\sqrt{\frac{3}{2}} m_{2,0}^{\text{ini}} \Omega_{\text{rf}}^2 (\Gamma^2 - 2\delta^2)}{16(\Gamma^2 + 4\delta^2) (\Gamma^2 + \delta^2)}, \quad (29)$$

$$D_2(\delta, \Omega_{\text{rf}} \approx 0) = \frac{3\sqrt{\frac{3}{2}} m_{2,0}^{\text{ini}} \Omega_{\text{rf}}^2 \Gamma \delta}{16(\Gamma^2 + 4\delta^2) (\Gamma^2 + \delta^2)}, \quad (30)$$

$$R_2(\delta, \Omega_{\text{rf}} \approx 0) = \frac{1}{16} \sqrt{\frac{3}{2}} m_{2,0}^{\text{ini}} \frac{\Omega_{\text{rf}}^2}{\sqrt{\Gamma^4 + 5\Gamma^2\delta^2 + 4\delta^4}}. \quad (31)$$

In our work we mainly focus on the signal at the first and second harmonics. However, for completeness, we also calculate the A_0 term which will give a DC rotation of the transmitted light polarization which in the limit of low RF intensities simplifies to

$$A_0(\delta, \Omega_{\text{rf}} \approx 0) = \sqrt{\frac{3}{2}} m_{2,0}^{\text{ini}} \left\{ \frac{1}{4} - \frac{3}{16} \frac{\Omega_{\text{rf}}^2}{(\Gamma^2 + \delta^2)} \right\}. \quad (32)$$

E. Absorption measurements

We now consider the light absorption signal. In the limit of low absorption, the transmitted light intensity will be $I(L) = I(0) \exp(-\kappa_{\text{abs}} L) \approx I(0) (1 - \kappa_{\text{abs}} L)$, where κ_{abs} is the absorption coefficient, L is the length of the vapour cell, and $I(0)$ and $I(L)$ are the light intensity before and after the vapour cell, respectively. The absorption coefficient can be calculated as [27, 30]

$$\kappa_{\text{abs}} \propto m'_{0,0} - \chi m'_{2,0}, \quad (33)$$

where again the prime refers to the multipoles defined with the quantization axis along the light-polarization direction. Here χ depends on the

hyperfine quantum number F . The first term in Eq. (33) is proportional to $m'_{0,0} = m_{0,0}$ and will give a constant offset. The second term, proportional to $m'_{2,0}$, will also lead to a DC absorption as well as absorption oscillating at frequencies ω_{rf} and $2\omega_{\text{rf}}$. We are mainly interested in the absorption at the first and second harmonics as those are measured in the experiments. Following the same procedure as in Sec. II D and then calculating $m'_{2,0}$, we find

$$S_1^{\text{abs}}(t) \propto f_1(\theta) [X_1 \cos(\omega_{\text{rf}} t) + Y_1 \sin(\omega_{\text{rf}} t)], \quad (34)$$

$$S_2^{\text{abs}}(t) \propto f_2(\theta) [X_2 \cos(2\omega_{\text{rf}} t) + Y_2 \sin(2\omega_{\text{rf}} t)], \quad (35)$$

where the angular dependence takes the form

$$f_1(\theta) = \sin(2\theta) [1 + 3 \cos(2\theta)] = h_2(\theta), \quad (36a)$$

$$f_2(\theta) = (1 - \cos(2\theta)) [1 + 3 \cos(2\theta)], \quad (36b)$$

and where the coefficients X_1, Y_1, X_2, Y_2 can be related to ones derived previously for the polarization rotation signal as follows

$$X_1 = -\frac{1}{4} \sqrt{6} D_1, \quad (37a)$$

$$Y_1 = -\frac{1}{4} \sqrt{6} A_1, \quad (37b)$$

$$X_2 = -\frac{1}{4} \sqrt{6} A_2, \quad (37c)$$

$$Y_2 = -\frac{1}{4} \sqrt{6} D_2. \quad (37d)$$

We see that the angular dependence for the absorption signal differs from that of the polarization rotation signal. However, the magnetic resonance lineshapes are the same for absorption and polarization rotation signals, up to a proportionality constant. Furthermore, our results for the absorption signals agree with what was calculated by Weis et al. [27]. Note that Ref. [27] considers a rotating RF field while we consider an RF field applied along one spatial direction, which leads to a factor of two difference in the definitions of the Rabi frequencies of the RF field.

III. EXPERIMENTAL SETUP

A schematic of the experimental setup for measuring magnetic resonance signals is shown in Fig. 2. A polarization maintaining optical fiber outputs linearly polarized light ($\lambda = 894.6$ nm) propagating in the y -direction. The light frequency is resonant with D1 transition ($F = 4 \rightarrow F' = 3$) of Cs atoms. The first pair of half waveplate and polarizing beamsplitter is used to minimise the polarization fluctuation of light whereas the second pair is used to control the incident

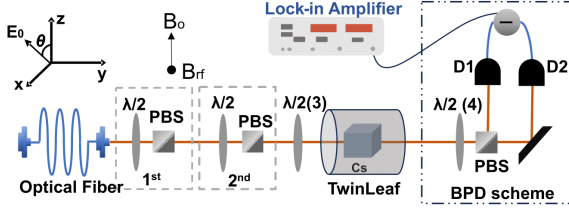


Figure 2: The schematic of experimental setup for the double resonance alignment magnetometry. Here $\lambda/2$ = Half waveplate, PBS = Polarizing beamsplitter, Twinleaf = Magnetic shield, Cs = Caesium vapour cell, BPD = Balanced photodetector, D1 and D2 are photodetectors.

light power. Another half waveplate $\lambda/2(3)$ is utilized to rotate the polarization angle (θ) of incident light in the zx -plane. The light, with an electric field amplitude E_0 , is then passed through a cubic paraffin coated Cs cell that is placed inside a four layered mu-metal magnetic shield (Twinleaf MS-1). For $\theta = 0$, the electric field amplitude is $\mathbf{E}_0 = E_0 \hat{\mathbf{z}}$ and for $\theta = 90^\circ$, we have $\mathbf{E}_0 = E_0 \hat{\mathbf{x}}$. A static magnetic field \mathbf{B}_0 is applied in the z -direction using a coil integrated in the Twinleaf magnetic shield. An oscillating weak RF magnetic field ($\mathbf{B}_{\text{rf}} = B_1 \cos(2\pi f_{\text{rf}} t) \hat{\mathbf{x}}$) is applied in the x -direction using a homemade coil placed inside the magnetic shield. Here $f_{\text{rf}} = \omega_{\text{rf}}/2\pi$ is the RF frequency in Hz. After the magnetic shield, a polarimetric technique based on balanced photodetection (BPD) using a half-wave plate $\lambda/2(4)$, a polarizing beamsplitter and a balanced photodetector (Thorlabs PDB210A/M) is employed to measure the polarization rotation of light. The output from the photodetector is then fed to a lock-in amplifier (Stanford Research Systems SR-830), which demodulates the signal for an adjusted harmonic. The in-phase (X) and quadrature (Y) signals are subsequently recorded using a data-acquisition card (Spectrum M2P.5932-X4) for further analysis. Note that for the absorption measurement, the BPD scheme is replaced by a single photodetector (Thorlabs PDA36A2).

IV. RESULTS AND DISCUSSION

A. Experimental procedure

We commence the discussion with the measurement of magnetic resonance signal. For these measurements, the static magnetic field strength is set to a value corresponding to a Larmor frequency of $f_L = \omega_L/2\pi \approx 9.5$ kHz. The frequency of the RF field is then swept from 8–12 kHz in 5 s. The polarization rotation of light is detected

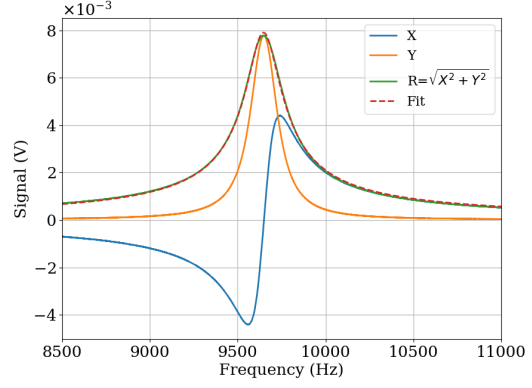


Figure 3: Example magnetic resonance signal for first harmonic observed through polarization rotation where light power is $P = 6 \mu\text{W}$, lock-in sensitivity = 10 mV and incident light polarization angle $\theta = 0^\circ$. The dashed lines are curve fitted to the data R.

with the balanced photodetector which is then demodulated by the lock-in amplifier to measure the in-phase and quadrature components. The time constant is set to 10 ms for all measurements. At the onset of measurement, the phase of the lock-in is adjusted to get the dispersive curve crossing the zero at resonant frequency for the incident polarization angle of $\theta = 0^\circ$. Subsequently, the lock-in phase was kept fixed throughout the measurements. A typical measurement of an in-phase (X) and quadrature (Y) signal for the first harmonic observed through polarization rotation is shown in Fig. 3. Note that while analyzing data, the lock-in sensitivity (which determines the gain of the lock-in amplifier) is taken into account, such that the plotted voltage in Fig. 3 corresponds to the root-mean square amplitude of the oscillating input signal to the lock-in amplifier. The figure also shows the calculated amplitude $R = \sqrt{X^2 + Y^2}$ which is fitted to Eq. (25).

In order to capture the angular dependence of resonance signal at first and second harmonic, the half-wave plates ($\lambda/2(3)$) and ($\lambda/2(4)$) are mounted in motorized rotation stages (Thorlabs PRM1-Z8) with dc controllers (Thorlabs KDC-101) and the angle is changed with a step size of 10° over a wider range of polarization angles (-20° to 110°). This experimental setting is repeated for different input light powers ($P = 1$ – $10 \mu\text{W}$). The magnetic resonance spectra was recorded and curve fitted to the Eq. (25) and Eq. (31) for the first and second harmonic, respectively. This allows us to extract the resonance frequency (where $f_{\text{rf}} = f_L$) in Hz, the relaxation rate $\Gamma/(2\pi)$ in Hz and the amplitude at resonance in Volts. Note that we used a single re-

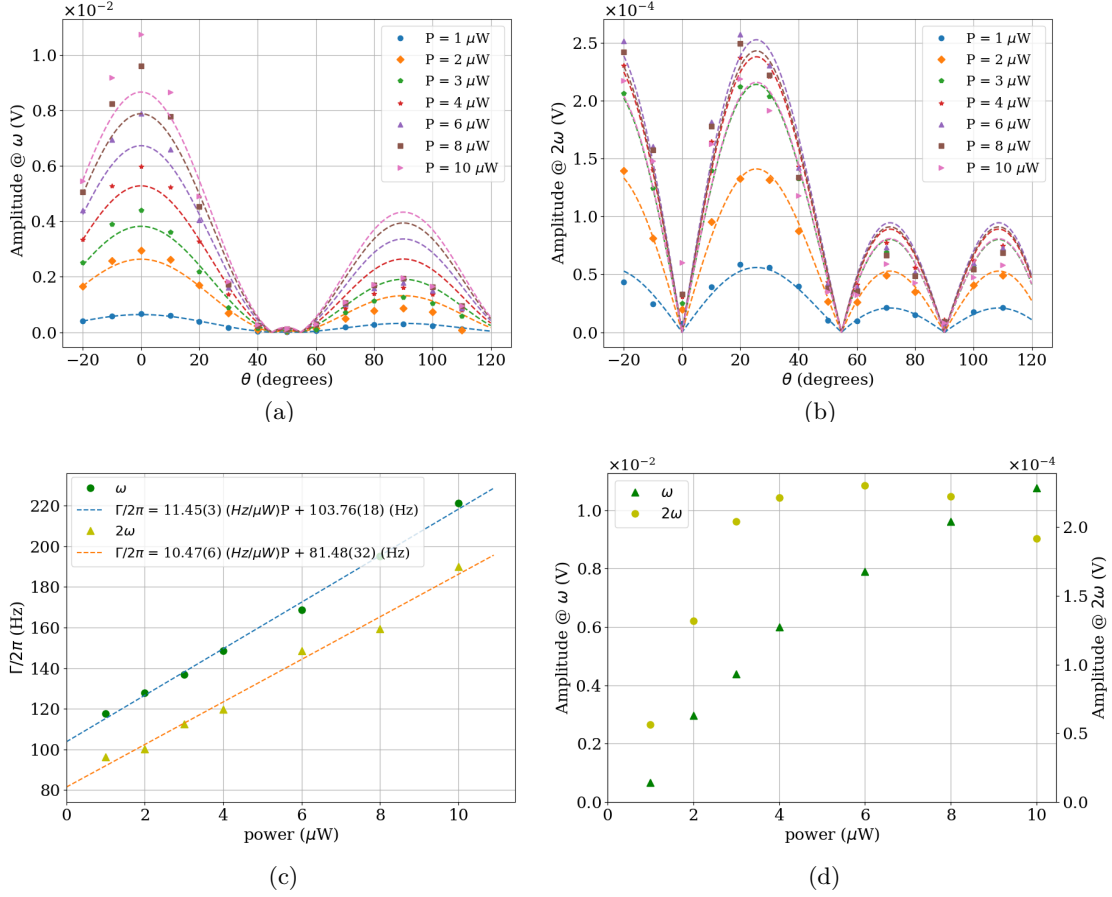


Figure 4: Polarization rotation measurement where on resonance amplitudes are plotted as a function of polarization angle of light for (a) first and (b) second harmonic. (c) Relaxation rate ($\Gamma/2\pi$) and (d) resonance signal amplitudes are depicted as a function of light power for first and second harmonic, respectively. The dashed lines are curve fit to the data.

laxation rate Γ for curve fitting which is contrary to the approach undertaken in Ref. [28]. Using an isotropic relaxation rate simplifies the analysis without undermining the theoretical framework. This experimental procedure is implemented for the measurement of both observables, i.e., intensity (absorption) and polarization rotation of light.

B. Angular dependence of resonance spectra

Fig. 4a and 4b shows the results for first and second harmonic where magnetic resonance spectra is observed through polarization rotation of the transmitted light. The extracted fit parameter amplitude has an angular dependence, dictated by Eq. (19b) and Eq. (19c) for first and second harmonic, respectively. It can be seen that experimental data fits reasonably well at the low powers of light. As the light power increases, ex-

perimental results tend to diverge from the theoretical description known to be valid only for weak probing.

Fig. 4c illustrates the fit parameter for the relaxation rate $\Gamma/2\pi$ as a function of light power. The data fits to a linear function $\Gamma/2\pi = c \cdot P + \Gamma_0/2\pi$ where c is the slope with units of $\text{Hz}/\mu\text{W}$ and $\Gamma_0/2\pi$ is the linewidth in Hz extrapolated to zero light power. Fig. 4d depicts the amplitude variation with input light power for a fixed value of polarization angle, i.e., $\theta = 0^\circ$ for first and $\theta = 20^\circ$ for second harmonic. It can be seen that the amplitude for first harmonic increases monotonically with the light power. However, for second harmonic, amplitude reaches a maximum value and then follows a downward trend with further increase of light power. This provides an useful insight to optimize the controlling parameters such as light power, polarization angle to maximize the sensitivity of OPM to be used in DRAM geometry.

Similarly, the measurement of the absorption

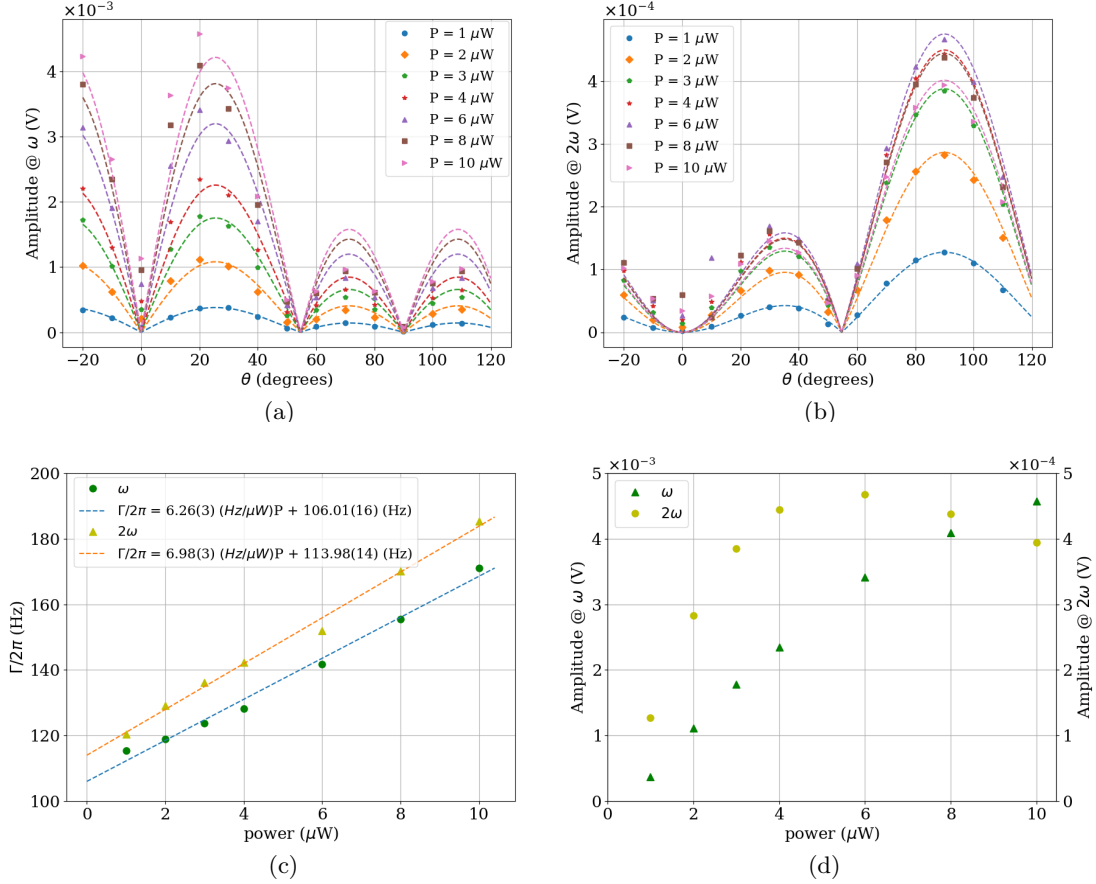


Figure 5: Absorption measurements where on resonance amplitude are plotted as a function of polarization angle of light for (a) first harmonic and (b) second harmonic whereas (c) relaxation rate ($\Gamma/2\pi$) and (d) on resonance amplitudes are plotted as a function of light power for first and second harmonic, respectively. The dashed lines are curve fit to the data.

of light is carried out for various input light powers and incident light polarization angles. Fig. 5a and 5b shows the angular dependence of the amplitude of absorption signal for first and second harmonic, respectively. In this case, the data is curve fitted to the Eq. (36a) and Eq. (36b) for the relevant harmonic. It is noticeable that the fit function for the first harmonic agrees with the experimental data at low light power but less so for the higher light powers. This is expected since the theoretical model is valid only for low light powers. Fig. 5c and 5d illustrates the relaxation rate and amplitude of the resonance spectra as a function of input light power for first and second harmonic, respectively. It can be seen that relaxation rate again has a linear relationship with input light power and is curve fitted to a similar function described earlier ($\Gamma/2\pi = c \cdot P + \Gamma_0/2\pi$). The variation in amplitude of resonance signal is similar to what we observe in Fig. 4d. However, it is noteworthy that amplitude value for first harmonic measured through polarization rotation is

approximately 2.3 times larger than amplitude measured in absorption signal. This underscores the enhanced sensitivity capability of polarization rotation based probing technique. Moreover, when measuring absorption and polarization rotation, the magnetic resonance signal reaches zero at specific polarization angles (θ) as dictated by the relevant equations (19b, 19c, 36a, 36b). However, we still observe small resonance signal at these angles. This small contribution can be ascribed to high light power.

C. Varying RF Amplitude

Eq. (22) and Eq. (28) capture the dependence of the magnetic resonance signal on the RF field amplitude for first and second harmonic, respectively. To validate the theory, we varied the RF field amplitude ($B_{\text{rf}} = gV_{\text{rf}}$) and measured the magnetic resonance spectra for both harmonics through polarization rotation measurement.

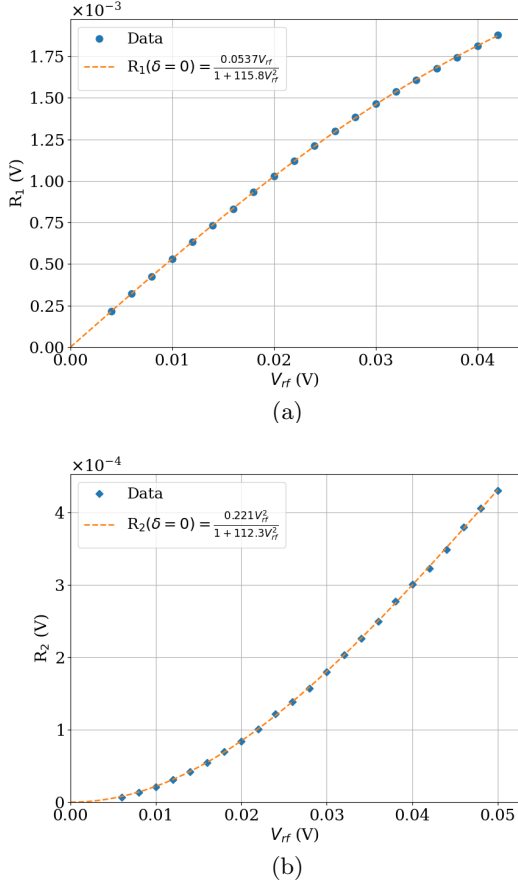


Figure 6: On resonance amplitude of magnetic resonance spectra is plotted as a function of RF voltage to the excitation coils for (a) first harmonic and (b) second harmonic. The dashed lines represent curve fit to the data.

Here g is the calibration factor with units (nT/V) and V_{rf} is the controlling parameter for RF field amplitude. For the excitation coils, the calibration factor (g) is determined and reads 210.8 nT/V. For incident polarization angle $\theta = 0$, the light power is fixed at $10 \mu\text{W}$ and Larmor frequency equals $f_L \approx 9.5 \text{ kHz}$. Subsequently, the resonance data is recorded and curve fitted to Eq. (22) and Eq. (28) for respective harmonic. The data is analyzed to extract the variable of interest such as amplitude (method as prescribed earlier in Section IV).

Fig. 6a and 6b capture the variations in amplitude of magnetic resonance signal as a function of applied RF voltage (V_{rf}) for first and second harmonic, respectively. The functions fit the experimental data reasonably well. For low values of RF power, the amplitude exhibits a linear and quadratic relationship with RF power for first and second harmonic, respectively. This respective dependence tend to diverge at higher values of

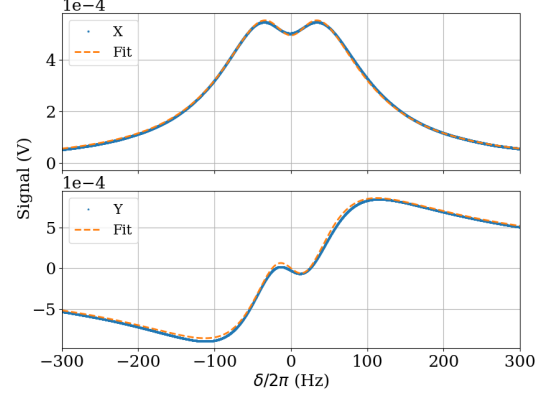


Figure 7: In-phase and quadrature magnetic resonance signal at higher amplitude of RF power plotted against the detuning δ . The resonance lineshapes are measured through polarization rotation where $P = 10 \mu\text{W}$, $\omega_L \approx 2\pi(9.5) \text{ kHz}$, $V_{rf} = 50 \text{ mV}$ and incident angle $\theta = 40^\circ$.

RF power, however Eq. (22) and Eq. (28) completely describe the variations in amplitudes for arbitrary strength of RF power. It is worth mentioning here that in accordance with the theoretical model at higher magnitudes of RF power, we noted an additional feature in the magnetic resonance spectra which appears at the resonance frequency. Fig. 7 illustrates the in-phase (X) and quadrature (Y) line spectra for high RF power. The in-phase and quadrature signals are fitted to the full expressions given by Eq. (20) and Eq. (21), respectively. The results are in good agreement with the theoretical findings.

It is pertinent to mention here that we also measured the magnetic resonance spectra in the earth's magnetic field range which gives the Larmor frequency of $\approx 175 \text{ kHz}$. The corresponding magnetic field is applied through a Twin-Leaf DC current source (CSU-1000). The observed lineshapes are presented in Fig. 8 where incident light polarization makes an angle 40° with the magnetic field \mathbf{B}_0 . We observed a large resonance peak at $\approx 175.36 \text{ kHz}$ and one additional small peak at the frequency $\approx 175.92 \text{ kHz}$ with a separation of $\approx 560 \text{ Hz}$. While the large resonance is due to atoms in the $F = 4$ hyperfine ground states, the small resonance is due to atoms in the $F = 3$ hyperfine ground states. This can be seen from the different gyromagnetic ratio of Cs for the $F = 3$ and $F = 4$ state, i.e., $g_{F=3}/g_{F=4} = -1.0032$ [34]. This implies that if the $F = 4$ resonance is at 175.36 kHz then the $F = 3$ resonance should be at $-1.0032 \times 175.36 \text{ kHz} = -175.92 \text{ kHz}$. The minus sign signifies that the resonance lineshapes for two ground

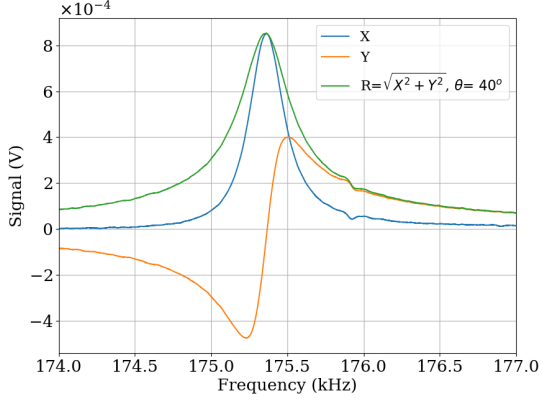


Figure 8: Magnetic resonance spectra observed through polarization rotation of the light in the geo-magnetic field range which corresponds to a Larmor frequency of ≈ 175 kHz with light power $P = 10 \mu\text{W}$.

states will be 180° out of phase with respect to each other and can be observed in Fig. 8. The $F = 3$ resonance is small since the laser is 9.2 GHz detuned from $F = 3$ resonance. This peak is not observable in the resonance spectra at 9.5 kHz since $9.5 \text{ kHz} \times 1.0032 = 9.530 \text{ KHz}$ and falls inside the large resonance peak.

D. Sensitivity Measurement

Figure 9a and 9b shows an RF frequency sweep with $f_L = 9.5$ kHz for absorption and polarization rotation measurement, respectively. For an applied oscillating field of 6.324 nT, the peak value of the resonance spectra is extracted and is subsequently divided by the RF magnetic field to give a conversion factor between the lock-in amplifier readout and the corresponding RF field amplitudes. For absorption measurement, it reads $R_A = (0.69(2) \text{ mV/nT})$ whereas for polarization signal, it is given by $R_{PR} = (2.12(3) \text{ mV/nT})$. We see that the polarization rotation signal is approximately a factor of three larger than for the absorption measurement. Note that the transimpedance gains of the two detectors are almost identical ($4.75 \cdot 10^5 \text{ V/A}$ and $5.0 \cdot 10^5 \text{ V/A}$). The RF frequency is then fixed to the Larmor frequency, i.e., $f_{\text{rf}} = f_L$, and a 4 minute time trace is obtained. This measurement is repeated with RF amplitude set to zero, i.e., “RF off”. The recorded data is then analysed to estimate the sensitivity of OPM for oscillating magnetic fields by the method prescribed in [35] where standard deviation of $240 \times 1 \text{ s}$ averaged segments is calculated. Fig. 9c shows the sensitivity to small oscillating magnetic fields for ab-

sorption detection mode and reads $3.02 \text{ pT}/\sqrt{\text{Hz}}$ for X and $3.18 \text{ pT}/\sqrt{\text{Hz}}$ for Y . Similarly, sensitivity measurement from polarization rotation is performed and results are presented in Fig. 9d. The magnetic field sensitivity for the X and Y are $\approx 0.35 \text{ pT}/\sqrt{\text{Hz}}$ and $\approx 0.36 \text{ pT}/\sqrt{\text{Hz}}$, respectively. Note that the sensitivity to magnetic field (δB_{meas}) measured through polarization rotation is approximately an order of magnitude better than absorption measurement.

In order to identify the intrinsic noise sources in the system, the light hitting the photodetector (Thorlabs PDB210A/M for the polarization rotation measurements and Thorlabs PDA36A2 for the absorption measurements) is blocked and another time trace is recorded (data not shown). The noise with the light blocked is $0.25 \text{ pT}/\sqrt{\text{Hz}}$ (for both X and Y) for the polarization measurement and $1.34 \text{ pT}/\sqrt{\text{Hz}}$ for the absorption measurement. This noise contribution is due to the electronic noise of the photodetector and data acquisition card.

To augment the analysis, we calculated the shot noise estimation for both detection modalities and details are presented in Appendix C. The estimated shot noise values are $0.80 \text{ pT}/\sqrt{\text{Hz}}$ and $0.26 \text{ pT}/\sqrt{\text{Hz}}$ for single and balanced photodetector, respectively. The fundamental limit to the sensitivity of an OPM is given by spin projection noise which is given by

$$\delta B_{\text{proj}} = \frac{2\hbar}{g_F \mu_B \sqrt{n V T_2}}, \quad (38)$$

where μ_B is the Bohr magneton, $g_F = 1/4$ for the $F = 4$ Cs ground state, $n \approx 2.2 \times 10^{16} \text{ m}^{-3}$ is the number density of Cs atoms at room temperature (18.5°C) [35] and $V = (5\text{mm})^3$ is the volume of our vapour cell. T_2 is the transverse relaxation time and is calculated as $T_2 = 1/2\pi\Gamma \approx 4.5 \text{ ms}$ for polarization rotation and $T_2 = 5.8 \text{ ms}$ for absorption measurement. Here we used the Γ values from Fig. 4c and Fig. 5c. The estimated spin projection noise for the absorption and polarization rotation measurements are $23 \text{ fT}/\sqrt{\text{Hz}}$ and $26 \text{ fT}/\sqrt{\text{Hz}}$, respectively. The measured magnetic field sensitivities and electronic noise, along with the estimated shot noise and projection noise are presented in Table. I. Moreover, we measured the light noise power spectral density with balanced and single photodetectors, see App. D (Fig. 10a and 10b). The average of the data in frequency range of interest (9–10.5 kHz) is taken and plotted as a function of optical power. It can be seen that for polarization measurements (Fig. 10c), using a balanced photodetector, one can achieve a shot-noise limited measurement (as seen from the linear dependence on light power) whereas for absorption measurements (Fig. 10d) with a sin-

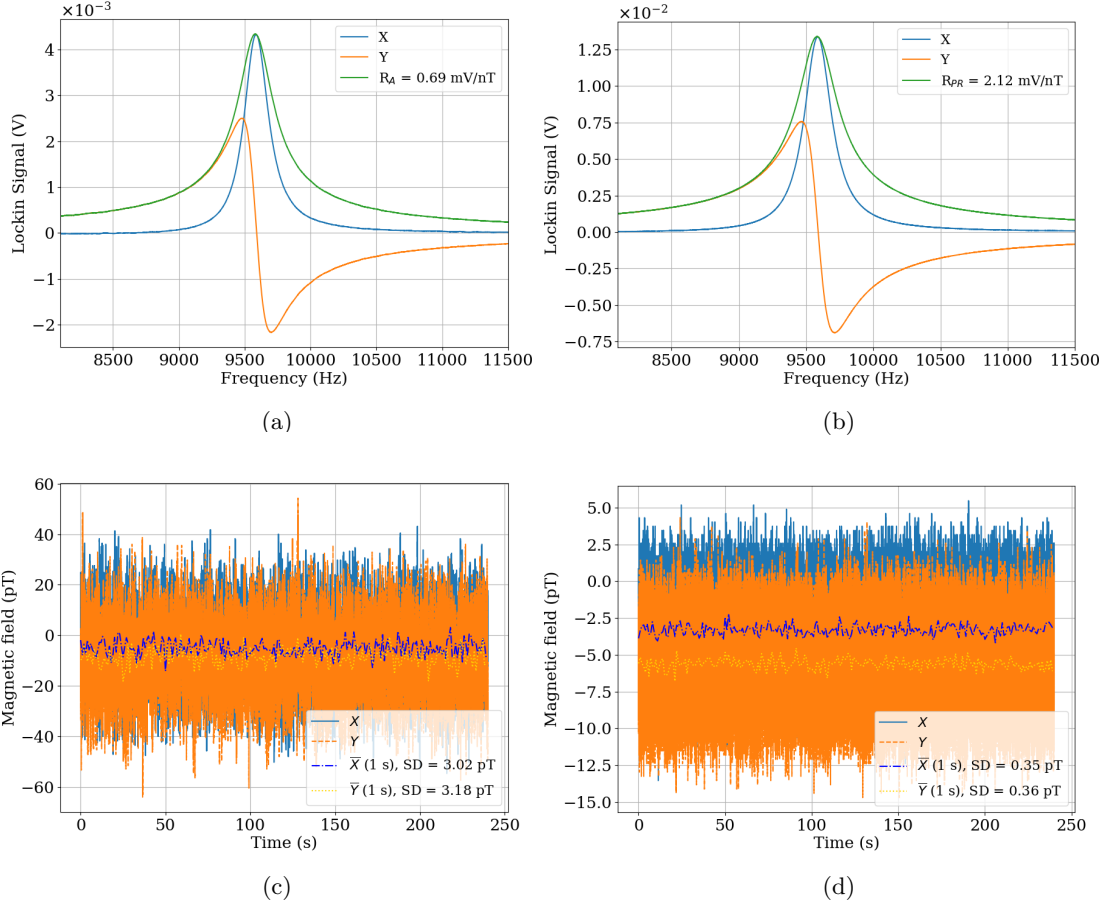


Figure 9: First harmonic signal for in-phase, quadrature, and signal R measured through (a) absorption and (b) polarization rotation measurement, whereas (c) and (d) show their respective sensitivities of the magnetic field. The light power is $10 \mu\text{W}$ and incident polarization angle is $\theta = 25^\circ$ and $\theta = 0^\circ$ for absorption and polarization rotation, respectively.

(pT/ $\sqrt{\text{Hz}}$)	δB_{meas}	δB_{Elec}	δB_{Shot}	δB_{proj}
Absorption	3.0	1.34	0.80	0.023
Polarization	0.35	0.25	0.26	0.026

Table I: Magnetic field sensitivities for the alignment based paraffin coated Cs cell OPM where δB_{meas} is the measured sensitivity to magnetic field and δB_{Elec} is the electronic noise whereas δB_{shot} is the estimated shot noise and δB_{proj} is the estimated projection noise.

gle detector, one will measure classical/technical light noise (as seen from the quadratic dependence on light power). We emphasize that the polarization rotation measurement yields better magnetic field sensitivity, approximately an order of magnitude in our experimental setting, than the absorption measurement. We note that the magnitude of spin projection noise is approximately identical for both techniques since the op-

tical pumping and evolution of atomic ensemble remains the same. Moreover, the signal amplitude and the sensitivity to magnetic field can be improved by heating the vapour cell.

V. CONCLUSION

In this study, we present theoretical description for polarized atomic ensemble for double resonance alignment magnetometer. We derive the analytical expressions for first and second harmonic signals where magnetic resonance spectra is accessed through polarization rotation and absorption of transmitted light through polarized atomic (Cs) vapours. The magnetic resonance spectra is investigated for various input parameters such as RF-field amplitude, input light power, angle between the magnetic field and the linear light polarization. The experimental results demonstrate a good agreement with the-

oretical findings. Furthermore, the sensitivity measurements are performed with both detection modalities, i.e., absorption and polarization rotation. It is found that polarization rotation offers better sensitivity, approximately an order of magnitude, than absorption measurement. Moreover if experimental setting is limited by shot noise, the sensitivity through polarization rotation is better by a factor of 3. Our results motivate the use of polarization rotation detection modality for prototype alignment based magnetometers, given the better sensitivity despite the added complexity in the experimental setup.

ACKNOWLEDGMENTS

This work was supported by the QuantERA grant C'MON-QSENS! funded by the Engineering and Physical Sciences Research Council (EPSRC) Grant No. EP/T027126/1, the EPSRC Grant No. EP/Y005260/1, the Novo Nordisk Foundation (Grant No. NNF20OC0064182). Project C'MON-QSENS! is supported by the National Science Centre (2019/32/Z/ST2/00026), Poland under QuantERA, which has received funding from the European Union's Horizon 2020 research and innovation programme under grant agreement no. 731473.

Appendix A: Angular Momentum Matrices

$$J_x^{(2)} = \hbar \begin{pmatrix} 0 & 1 & 0 & 0 & 0 \\ 1 & 0 & \sqrt{\frac{3}{2}} & 0 & 0 \\ 0 & \sqrt{\frac{3}{2}} & 0 & \sqrt{\frac{3}{2}} & 0 \\ 0 & 0 & \sqrt{\frac{3}{2}} & 0 & 1 \\ 0 & 0 & 0 & 1 & 0 \end{pmatrix}, \quad (\text{A1})$$

$$J_y^{(2)} = \hbar \begin{pmatrix} 0 & i & 0 & 0 & 0 \\ -i & 0 & i\sqrt{\frac{3}{2}} & 0 & 0 \\ 0 & -i\sqrt{\frac{3}{2}} & 0 & i\sqrt{\frac{3}{2}} & 0 \\ 0 & 0 & -i\sqrt{\frac{3}{2}} & 0 & i \\ 0 & 0 & 0 & -i & 0 \end{pmatrix}, \quad (\text{A2})$$

$$J_z^{(2)} = \hbar \begin{pmatrix} -2 & 0 & 0 & 0 & 0 \\ 0 & -1 & 0 & 0 & 0 \\ 0 & 0 & 0 & 0 & 0 \\ 0 & 0 & 0 & 1 & 0 \\ 0 & 0 & 0 & 0 & 2 \end{pmatrix}. \quad (\text{A3})$$

Appendix B: Steady state rotating frame multipoles

The steady state multipole $\tilde{\mathbf{m}}_2^{\text{ss}}$ in the rotating frame has the following components

$$\tilde{m}_{2,-2}^{\text{ss}} = \frac{-\sqrt{\frac{3}{2}} m_{2,0}^{\text{eq}}(\theta) \Omega_{\text{rf}}^2 [4(\Gamma - i\delta)(\Gamma - 2i\delta) + \Omega_{\text{rf}}^2]}{4(\Gamma^2 + 4\delta^2 + \Omega_{\text{rf}}^2) [4(\Gamma^2 + \delta^2) + \Omega_{\text{rf}}^2]}, \quad (\text{B1})$$

$$\tilde{m}_{2,-1}^{\text{ss}} = \frac{-i\sqrt{\frac{3}{2}} m_{2,0}^{\text{eq}}(\theta) (\Gamma + 2i\delta) \Omega_{\text{rf}} [4(\Gamma - i\delta)(\Gamma - 2i\delta) + \Omega_{\text{rf}}^2]}{2(\Gamma^2 + 4\delta^2 + \Omega_{\text{rf}}^2) [4(\Gamma^2 + \delta^2) + \Omega_{\text{rf}}^2]}, \quad (\text{B2})$$

$$\tilde{m}_{2,0}^{\text{ss}} = \frac{m_{2,0}^{\text{eq}}(\theta) [16(\Gamma^2 + \delta^2)(\Gamma^2 + 4\delta^2) + 8(\Gamma^2 - 2\delta^2)\Omega_{\text{rf}}^2 + \Omega_{\text{rf}}^4]}{4(\Gamma^2 + 4\delta^2 + \Omega_{\text{rf}}^2) [4(\Gamma^2 + \delta^2) + \Omega_{\text{rf}}^2]}, \quad (\text{B3})$$

$$\tilde{m}_{2,1}^{\text{ss}} = \frac{-i\sqrt{\frac{3}{2}} m_{2,0}^{\text{eq}}(\theta) (\Gamma - 2i\delta) \Omega_{\text{rf}} [4(\Gamma + i\delta)(\Gamma + 2i\delta) + \Omega_{\text{rf}}^2]}{2(\Gamma^2 + 4\delta^2 + \Omega_{\text{rf}}^2) [4(\Gamma^2 + \delta^2) + \Omega_{\text{rf}}^2]}, \quad (\text{B4})$$

$$\tilde{m}_{2,2}^{\text{ss}} = \frac{-\sqrt{\frac{3}{2}} m_{2,0}^{\text{eq}}(\theta) \Omega_{\text{rf}}^2 [4(\Gamma + i\delta)(\Gamma + 2i\delta) + \Omega_{\text{rf}}^2]}{4(\Gamma^2 + 4\delta^2 + \Omega_{\text{rf}}^2) [4(\Gamma^2 + \delta^2) + \Omega_{\text{rf}}^2]}. \quad (\text{B5})$$

Appendix C: Shot Noise Estimation

The shot noise for a photodetector is given by $\Delta i / \sqrt{\Delta f} = \sqrt{2eI}$ where e is the electronic charge,

$I = R(\lambda)P$ is the average current from the photodetector with $R(\lambda)$ as responsivity and P is the incident light power on the detector. For 10 μW light measured before the vapour cell, and an es-

timated 73% transmission of light through the vapour cell, the power on the single detector will be $7.3 \mu\text{W}$. This gives a shot noise estimation in $\text{A}/\sqrt{\text{Hz}}$. Since the detector output is in volts and we also measure voltage signal with the lock-in, it is more useful to write the formula for shot noise in terms of $\text{V}/\sqrt{\text{Hz}}$ which reads as follows

$$\frac{\Delta V}{\sqrt{\Delta f}} = \frac{\Delta i}{\sqrt{\Delta f}} (G \times S.F), \quad (\text{C1})$$

where G is the trans-impedance amplifier (TIA) gain of the photodetector and $S.F$ is the scale factor which equals ≈ 1 due to high impedance of lock-in input channel. For absorption technique, the estimated shot noise at $P = 10 \mu\text{W}$ then reads $\approx 5.6 \times 10^{-3} \text{ V}/\sqrt{\text{Hz}}$ where we have also taken into account the internal gain of lock-in amplifier. The value of shot noise is then subsequently divided by the conversion factor RA to convert the shot noise ($\text{V}/\sqrt{\text{Hz}}$) in units of magnetic

field and reads $0.80 \text{ pT}/\sqrt{\text{Hz}}$. Similar calculations were performed for the balanced photodetector by taking into account the respective gain and responsivity of the detector, the transmission through the vapour cell and a further estimated transmission of 92% through the polarizing beam-splitter. Subsequently, the value of shot noise is divided by the conversion factor R_{PR} and the estimated shot noise reads $0.26 \text{ pT}/\sqrt{\text{Hz}}$.

Appendix D: Power Spectral Density Measurement

For different input light power, time traces were obtained. The power spectral density (PSD) of each trace is obtained. The PSD trace data is split into 50 time traces and subsequently, average of power spectral densities is taken and plotted.

-
- [1] Dmitry Budker and Michael Romalis. Optical magnetometry. *Nature physics*, 3(4):227–234, 2007.
 - [2] D. Budker and D.F.J. Kimball. *Optical Magnetometry*. Cambridge University Press, 2013.
 - [3] Reuben Benumof. Optical pumping theory and experiments. *Am. J. Phys.*, 33(2):151–160, 1965.
 - [4] H Xia, Andrei Ben-Amar Baranga, D Hoffman, and MV Romalis. Magnetoencephalography with an atomic magnetometer. *Appl. Phys. Lett.*, 89(21):211104, 2006.
 - [5] TH Sander, J Preusser, R Mhaskar, J Kitching, L Trahms, and S Knappe. Magnetoencephalography with a chip-scale atomic magnetometer. *Biomed. Opt. Express*, 3(5):981–990, 2012.
 - [6] Amir Borna, Tony R Carter, Josh D Goldberg, Anthony P Colombo, Yuan-Yu Jau, Christopher Berry, Jim McKay, Julia Stephen, Michael Weisend, and Peter DD Schwindt. A 20-channel magnetoencephalography system based on optically pumped magnetometers. *Phys. Med. Biol.*, 62(23):8909, 2017.
 - [7] Joonas Iivanainen, Rasmus Zetter, Mikael Grön, Karoliina Hakkarainen, and Lauri Parkkonen. On-scalp meg system utilizing an actively shielded array of optically-pumped magnetometers. *Neuroimage*, 194:244–258, 2019.
 - [8] Matthew J Brookes, James Leggett, Molly Rea, Ryan M Hill, Niall Holmes, Elena Boto, and Richard Bowtell. Magnetoencephalography with optically pumped magnetometers (opm-meg): the next generation of functional neuroimaging. *Trends Neurosci.*, 2022.
 - [9] Kasper Jensen, Mark Alexander Skarsfeldt, Hans Stærkind, Jens Arnbak, Mikhail V Balabas, Søren-Peter Olesen, Bo Hjorth Bentzen, and Eugene S Polzik. Magnetocardiography on an isolated animal heart with a room-temperature optically pumped magnetometer. *Sci. Rep.*, 8(1):16218, 2018.
 - [10] Kasper Jensen, Bo Hjorth Bentzen, and Eugene S Polzik. Small animal biomagnetism applications. In *Flexible High Performance Magnetic Field Sensors: On-Scalp Magnetoencephalography and Other Applications*, pages 33–48. Springer, 2022.
 - [11] W. Chalupczak, R. M. Godun, S. Pustelny, and W. Gawlik. Room temperature femtotesla radio-frequency atomic magnetometer. *Appl. Phys. Lett.*, 100(24):242401, 2012.
 - [12] Anna U Kowalczyk, Yulia Bezsudnova, Ole Jensen, and Giovanni Barontini. Detection of human auditory evoked brain signals with a resilient nonlinear optically pumped magnetometer. *NeuroImage*, 226:117497, 2021.
 - [13] Michael V Romalis and Hoan B Dang. Atomic magnetometers for materials characterization. *Mat. Today. Phys.*, 14(6):258–262, 2011.
 - [14] Lucas M Rushton, Tadas Pyragius, Adil Meraki, Lucy Elson, and Kasper Jensen. Unshielded portable optically pumped magnetometer for the remote detection of conductive objects using eddy current measurements. *Rev. Sci. Instrum.*, 93(12), 2022.
 - [15] Cameron Deans, Luca Marmugi, and Ferruccio Renzoni. Active underwater detection with an array of atomic magnetometers. *Applied optics*, 57(10):2346–2351, 2018.
 - [16] Hector Masia-Roig, Joseph A Smiga, Dmitry Budker, Vincent Dumont, Zoran Grujic, Dongok Kim, Derek F Jackson Kimball, Victor Lebedev, Madeline Monroy, Szymon Pustelny, et al. Analysis method for detecting topological defect dark matter with a global magnetometer net-

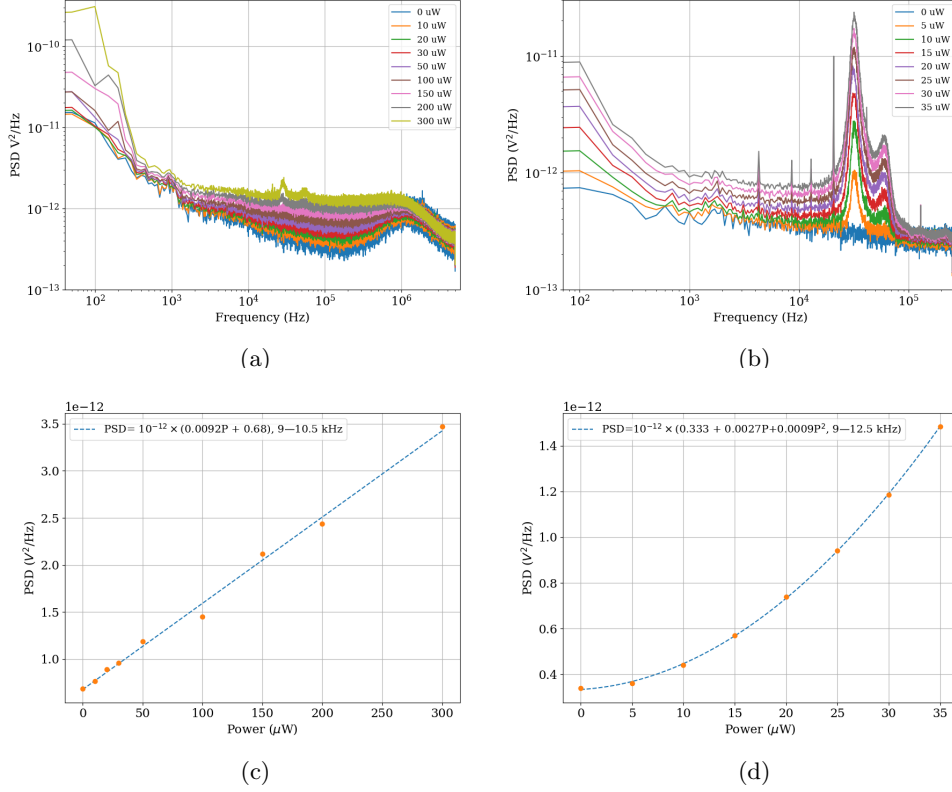


Figure 10: PSD with (a) balanced detector and (b) single photodetector. The average PSD in the frequency range 9–10.5 kHz is plotted as a function of optical power for (c) balanced and (d) single photodetector.

- work. *Phy. Dark Universe*, 28:100494, 2020.
- [17] M Pospelov, Szymon Pustelny, MP Ledbetter, DF Jackson Kimball, Wojciech Gawlik, and D Budker. Detecting domain walls of axionlike models using terrestrial experiments. *Phys. Rev. Lett.*, 110(2):021803, 2013.
 - [18] Binbin Zhao, Lin Li, Yaohua Zhang, Junjian Tang, Ying Liu, and Yueyang Zhai. Optically pumped magnetometers recent advances and applications in biomagnetism: A review. *IEEE Sens. J.*, 2023.
 - [19] Carmine Granata and Antonio Vettoliere. Nano superconducting quantum interference device: A powerful tool for nanoscale investigations. *Phys. Rep.*, 614:1–69, 2016.
 - [20] Richard J Clancy, Vladislav Gerginov, Orang Alem, Stephen Becker, and Svenja Knappe. A study of scalar optically-pumped magnetometers for use in magnetoencephalography without shielding. *Phys. Med. Biol.*, 66(17):175030, 2021.
 - [21] ME Limes, EL Foley, TW Kornack, S Caliga, S McBride, A Braun, W Lee, VG Lucivero, and MV Romalis. Portable magnetometry for detection of biomagnetism in ambient environments. *Phys. Rev. Appl.*, 14(1):011002, 2020.
 - [22] Natalie Rhodes, Niall Holmes, Ryan Hill, Gareth Barnes, Richard Bowtell, Matthew Brookes, and Elena Boto. Turning opm-meg into a wearable technology. In *Flexible High Performance Magnetic Field Sensors: On-Scalp Magnetoencephalography and Other Applications*, pages 195–223. Springer, 2022.
 - [23] Arjan Hillebrand, Niall Holmes, Ndedi Sijsma, George C Oâ€™Neill, Tim M Tierney, Niels Liberton, Anine H Stam, Nicole van Klink, Cornelis J Stam, Richard Bowtell, et al. Non-invasive measurements of ictal and interictal epileptiform activity using optically pumped magnetometers. *Sci. Rep.*, 13(1):4623, 2023.
 - [24] A. Weis, G Bison, and Z. D. Grujić. Magnetic resonance based atomic magnetometers. In A. Grosz, M. J. Haji-Sheikh, and S. C. Mukhopadhyay, editors, *High Sensitivity Magnetometers*, chapter 13. Springer Cham, 2016.
 - [25] P Bevington, R Gartman, and W Chalupczak. Enhanced material defect imaging with a radio-frequency atomic magnetometer. *J. Appl. Phys.*, 125(9), 2019.
 - [26] P Bevington, R Gartman, DJ Botelho, R Crawford, M Packer, TM Fromhold, and W Chalupczak. Object surveillance with radio-frequency atomic magnetometers. *Rev. Sci. Instrum.*, 91(5), 2020.
 - [27] Antoine Weis, Georg Bison, and Anatoly S Pazgalev. Theory of double resonance magnetometers based on atomic alignment. *Phys. Rev. A*,

- 74(3):033401, 2006.
- [28] Gianni Di Domenico, Georg Bison, Stephan Groeger, Paul Knowles, Anatoly S Pazgalev, Martin Rebetez, Hervé Saudan, and Antoine Weis. Experimental study of laser-detected magnetic resonance based on atomic alignment. *Phys. Rev. A*, 74(6):063415, 2006.
 - [29] Gianni Di Domenico, Hervé Saudan, Georg Bison, Paul Knowles, and Antoine Weis. Sensitivity of double-resonance alignment magnetometers. *Phys. Rev. A*, 76(2):023407, 2007.
 - [30] Adil Meraki, Lucy Elson, Nok Ho, Ali Akbar, Marcin Kozbial, Jan Kolodyński, and Kasper Jensen. Zero-field optical magnetometer based on spin alignment. *Physical Review A*, 108(6):062610, 2023.
 - [31] Stuart J Ingleby, Carolyn O’Dwyer, Paul F Griffin, Aidan S Arnold, and Erling Riis. Vector magnetometry exploiting phase-geometry effects in a double-resonance alignment magnetometer. *Physical Review Applied*, 10(3):034035, 2018.
 - [32] Marcin Kozbial, Lucy Elson, Lucas M Rushton, Ali Akbar, Adil Meraki, Kasper Jensen, and Jan Kolodyński. Spin noise spectroscopy of an alignment-based atomic magnetometer. *arXiv preprint arXiv:2312.05577*, 2023.
 - [33] M. Auzinsh, D. Budker, and S. M. Rochester. *Optically Polarized Atoms*. Oxford University Press, 2010.
 - [34] D. A. Steck. Cs d line data. <https://steck.us/alkalidata/cesiumnumbers.1.6.pdf>, July 2023.
 - [35] Lucas M Rushton, Lucy Elson, Adil Meraki, and Kasper Jensen. Alignment-Based Optically Pumped Magnetometer Using a Buffer-Gas Cell. *Phys. Rev. Appl.*, 19(6):064047, 2023.